



Papers published in *Ocean Science Discussions* are under  
open-access review for the journal *Ocean Science*

**OSD**

4, 371–398, 2007

---

**Internal tides and  
energy fluxes over  
Great Meteor  
Seamount**

T. Gerkema and  
H. van Haren

---

# **Internal tides and energy fluxes over Great Meteor Seamount**

**T. Gerkema and H. van Haren**

Royal NIOZ, P.O. Box 59, 1790 AB Den Burg, Texel, The Netherlands

Received: 1 March 2007 – Accepted: 23 March 2007 – Published: 3 April 2007

Correspondence to: T. Gerkema (gerk@nioz.nl)

[Title Page](#)

[Abstract](#)

[Introduction](#)

[Conclusions](#)

[References](#)

[Tables](#)

[Figures](#)

[◀](#)

[▶](#)

[◀](#)

[▶](#)

[Back](#)

[Close](#)

[Full Screen / Esc](#)

[Printer-friendly Version](#)

[Interactive Discussion](#)

## Abstract

Internal-tide energy fluxes are determined halfway over the southern slope of Great Meteor Seamount (Canary Basin), using data from combined CTD/LADCP yoyoing, covering the whole water column. The strongest signal is semi-diurnal and is concentrated in the upper few hundred meters of the water column. An indeterminacy in energy flux profiles is discussed; it is argued that a commonly applied condition used to uniquely determine these profiles does in fact not apply over sloping bottoms. However, the vertically integrated flux can be established unambiguously. The observed results are compared to the outcome of a numerical internal-tide generation model. For the semi-diurnal internal tide, the vertically integrated flux found in the model corresponds well to the observed one. For the diurnal tide, however, the former is much smaller; this points to non-tidal origins of the diurnal signal, which is indeed to be expected at this latitude ( $30^{\circ}$ ), where near-inertial and diurnal periods coincide.

## 1 Introduction

Recent estimates, based on satellite altimetry and modelling, indicate that barotropic tides lose about one third of their energy in the deep ocean (Egbert and Ray, 2003); this loss occurs predominantly over rough topography. From these findings, supplemented by in-situ observations, one can infer that the principal process responsible for this loss is internal-tide generation, a process in which energy is transferred from barotropic to baroclinic tides. Observations at the Hawaiian Ridge support this idea; internal-tide energy fluxes of the order of  $10 \text{ kW m}^{-1}$  were found at various locations (Rainville and Pinkel, 2006; Nash et al., 2006), and the total loss of barotropic tidal energy, for all the tidal constituents together, in the near-Hawaiian area is estimated at nearly 25 GW (Zaron and Egbert, 2006). Of this amount, an estimated 15% is lost to turbulence in the vicinity of the ridge, presumably by cascading of internal-tide energy to smaller scales (Klymak et al., 2006).

OSD

4, 371–398, 2007

---

## Internal tides and energy fluxes over Great Meteor Seamount

T. Gerkema and  
H. van Haren

---

[Title Page](#)

[Abstract](#)

[Introduction](#)

[Conclusions](#)

[References](#)

[Tables](#)

[Figures](#)

[◀](#)

[▶](#)

[◀](#)

[▶](#)

[Back](#)

[Close](#)

[Full Screen / Esc](#)

[Printer-friendly Version](#)

[Interactive Discussion](#)

In this paper, we present observations aimed at determining internal-tide energy fluxes over Great Meteor Seamount, which lies in the western part of the Canary Basin, halfway between the Canary Islands and the mid-Atlantic ridge. It is a *guyot*, named after the research vessel “*Meteor*” with which it was discovered in 1938 (Dietrich, 1970).  
5 An overview of the hydrography around this seamount was given by Mohn and Beckmann (2002), based on observational and modelling work. Besides a near southwestward flow, being part of the wind-driven subtropical gyre, they found semi-diurnal and diurnal barotropic and baroclinic tides (we discuss some of their specificities below). Moreover, they observed a sharp rise of the isopycnals near the slope. The time-  
10 variability of the bottom boundary layer was studied by van Haren (2005); in the course of minutes, a steep front or bore may pass, whose overturning diminishes the local stratification profoundly, but during the remainder of the tidal period the stratification is gradually reconstituted; overall, this cycle repeats itself every tidal period, but never exactly, so that there is a good deal of unpredictability in the stratification. The short time  
15 scales involved in this process impose an unusually high sampling rate and therefore require devices adapted for this purpose (van Haren et al., 2005).

Great Meteor Seamount covers, approximately, the latitudinal range 29.5–30.5° N. This fact renders the diurnal tidal signal particularly multi-faceted. The diurnal component  $K_1$ , whose critical latitude is 30.0° N, can exist as a free wave only at the southern flank of the seamount; the component  $O_1$ , on the other hand, with critical latitude 27.6° N, nowhere exists as a free wave, and hence must be trapped at both flanks. In both components, either free or trapped, energy may be converted from the barotropic to the baroclinic tide. This is one origin of diurnal internal tides at this location. Another mechanism is subharmonic resonance (Hibiya et al., 2002; MacKinnon and Winters,  
20 2005; Gerkema et al., 2006): semi-diurnal internal tides may by parametric subharmonic instability excite internal tides of half that frequency at latitudes where the latter can exist as a free waves (i.e. equatorward of 29.9° S/N for  $S_2$ , and 28.8° S/N for  $M_2$ ). For  $S_2$  this process may occur at the southern flank, but for  $M_2$  only at some southward distance from Great Meteor Seamount. (We note that in defining the “critical” latitude,  
25

## Internal tides and energy fluxes over Great Meteor Seamount

T. Gerkema and  
H. van Haren

[Title Page](#)

[Abstract](#)

[Introduction](#)

[Conclusions](#)

[References](#)

[Tables](#)

[Figures](#)

[◀](#)

[▶](#)

[◀](#)

[▶](#)

[Back](#)

[Close](#)

[Full Screen / Esc](#)

[Printer-friendly Version](#)

[Interactive Discussion](#)

we use the traditional definition according to which it is the latitude where the tidal frequency equals the local Coriolis parameter  $f$ ; in weakly stratified regions, such as the abyssal ocean, this definition requires modification, as pointed out by [Gerkema and Shrira \(2005\)](#); the actual critical latitude then lies further poleward, up to several degrees for the weakly stratified abyss.) All these frequencies lie indeed close to the local inertial frequency  $f$ , at which near-inertial waves occur due to atmospheric forcing and geostrophic adjustment. In the analysis presented here, which involves a time-series of two days, they cannot be distinguished, and are therefore considered collectively as the “diurnal” signal.

The basic definition of internal-tide energy flux is  $E_f = \langle up \rangle$ , where brackets denote the time-average over a tidal period;  $u$  and  $p$  are the baroclinic velocity component (in the direction of the energy flux) and baroclinic pressure, respectively. As it stands, this expression is unsuitable for practical purposes, because baroclinic pressure cannot be directly deduced from measurements. (However, the vertically integrated energy flux can be calculated straightforwardly.) To determine baroclinic pressure from isopycnal excursions, [Kunze et al. \(2002\)](#) proposed a “baroclinicity condition for pressure” to the effect that its vertical integral is assumed to be zero. Although they added a cautionary remark (“this condition may not hold in regions of direct forcing”), they did not in fact restrain its application to regions away from topography, nor did later authors ([Nash et al., 2005, 2006](#)); indeed, the condition has been indiscriminately applied over large canyons and ridges. In this paper we reconsider the validity of the condition, and probe into the reason why it does not, in general, hold over topography; we put forward as a cause of its failure the non-separable nature over topography rather than the “direct forcing” suggested by [Kunze et al. \(2002\)](#).

This paper is organized as follows. We present the measurements in Sect. 2, and apply a harmonic analysis on them in Sect. 3. In Sect. 4 we discuss the fundamental issues concerning energy fluxes (Sect. 4.1) and the results from the observations (Sect. 4.2). A comparison with a numerical internal-tide generation model is made in Sect. 5.

## Internal tides and energy fluxes over Great Meteor Seamount

T. Gerkema and  
H. van Haren

[Title Page](#)

[Abstract](#)

[Introduction](#)

[Conclusions](#)

[References](#)

[Tables](#)

[Figures](#)

[◀](#)

[▶](#)

[◀](#)

[▶](#)

[Back](#)

[Close](#)

[Full Screen / Esc](#)

[Printer-friendly Version](#)

[Interactive Discussion](#)

## 2 Measurements

The area of investigation is Great Meteor Seamount, centered around 30° N, 28.5° W. Simultaneous CTD and LADCP (Lowered Acoustic Doppler Current Profiler) yoyoing was carried out approximately halfway up its south-eastern slope, at the spot marked in Fig. 1, where the waterdepth is 1980 m. The measurements started at 08:45 UTC on 7 June 2006, and continued until 09:15 UTC the next day (van Haren, 2006); in the figures shown below, we refer to the start as  $t=0$ . In this timespan of 24.5 h, 20 casts were made.

The instrumental package was lowered and hoisted between 5 m from the surface and the bottom at a speed of about  $1 \text{ ms}^{-1}$ . The package consisted of a Sea-Bird 911plus CTD sampling at 24 Hz. For the present purposes, the CTD data were vertically subsampled at intervals of 0.5 dbar. On the same frame, two 300 kHz RDI ADCPs were mounted, one upward looking, the other, downward; together they form the LADCP. The ADCPs sampled currents at depth intervals between 8–20 m from their head at an accuracy of about  $0.05 \text{ ms}^{-1}$ .

### 2.1 Temperature and salinity

In the analysis of the temperature and salinity data, up- and down casts of the CTD were treated separately, making the total number of vertical profiles twice that of the number of casts. The data were interpolated to a regular time-grid with steps of half an hour, and vertically interpolated to a grid with  $\Delta z=0.5 \text{ m}$ . The time-averaged signal is shown in Figs. 2a, b. A conspicuous feature is the local salinity maximum at approximately 1100 m depth (accompanied by a less noticeable increase in temperature), which is due to the outflow of Mediterranean water.

The buoyancy frequency  $N$  can be determined using its basic definition

$$25 \quad N^2 = g^2 \left( \frac{d\rho}{dp} - \frac{1}{c_s^2} \right).$$

OSD

4, 371–398, 2007

## Internal tides and energy fluxes over Great Meteor Seamount

T. Gerkema and  
H. van Haren

[Title Page](#)

[Abstract](#)

[Introduction](#)

[Conclusions](#)

[References](#)

[Tables](#)

[Figures](#)

◀

▶

[Back](#)

[Close](#)

[Full Screen / Esc](#)

[Printer-friendly Version](#)

[Interactive Discussion](#)

5 Here  $\rho$  is the in-situ density and  $c_s$  the speed of sound; these quantities were calculated as functions of pressure, temperature and salinity using the equation of state for the Gibbs potential (Feistel and Hagen, 1995). The derivative  $d\rho/dp$  was approximated by discretization with steps  $\Delta p$  of 0.5 dbar. The time-averaged profile of  $N$  is shown in Fig. 2c. In a few instances,  $N^2$  is slightly negative; they are here rendered by  $N=0$ .

Having obtained the in-situ density  $\rho$  from the equation of state, we can calculate its time-averaged value  $\langle \rho \rangle$ , and hence buoyancy  $b$  by

$$b = -g \frac{\rho - \langle \rho \rangle}{\rho_*}, \quad (1)$$

10 where  $\rho_*$  is the mean of  $\langle \rho \rangle$  over the vertical. So,  $b$  represents the departure of density from its time-average, rescaled by a factor  $-g/\rho_*$ . The field  $b$ , as a function of vertical and time, is shown in Fig. 3a. The predominantly semi-diurnal character of the signal is obvious, especially in the upper part of the water column. Vertical isopycnal displacements  $\zeta$  can be derived from  $b$  via  $\zeta = -b/(N^2)$ , see Fig. 3b. Peak amplitudes as large as 75 m are reached at some points (for clearer representation, the amplitude-range is however restricted to 50 m in Fig. 3b). The stripiness of the signal through the vertical is due to small-scale variations in  $\langle N \rangle$ , cf. Fig. 2c. In the deeper parts of the water column, a weak quarter-diurnal signal is visible.

## 2.2 Currents

20 In the LADCP measurements the up- and downcasts were combined in the postprocessing to correct for systematic errors; hence the records provide 20 vertical profiles from the casts. The original set contains data every 20 m in the vertical, which we interpolated to a grid of  $\Delta z=0.5$  m for consistency with the CTD data and later handling. The horizontal velocity was decomposed into a cross-slope component  $u$ , taken along the dotted diagonal of Fig. 1 (positive in the north-eastern direction), and, perpendicularly to it, an along-slope component  $v$  (positive in the north-western direction).

## Internal tides and energy fluxes over Great Meteor Seamount

T. Gerkema and  
H. van Haren

[Title Page](#)

[Abstract](#)

[Introduction](#)

[Conclusions](#)

[References](#)

[Tables](#)

[Figures](#)

[◀](#)

[▶](#)

[◀](#)

[▶](#)

[Back](#)

[Close](#)

[Full Screen / Esc](#)

[Printer-friendly Version](#)

[Interactive Discussion](#)

Figure 4 shows the full signal  $u$  and  $v$ . Again the predominantly semi-diurnal character is clearly visible, while a shift to offslope currents is visible in the upper 400 m in Fig. 4a (blue dominates), indicative of a net background current; also, one finds in Fig. 4b that north-western currents are slightly dominant around 300 m (red dominates); these features, indicative of residual currents, are further illustrated in Fig. 5. The former fits in with the overall pattern of the eastern branch of the subtropical gyre (Mohn and Beckmann, 2002), while the latter may be due to tidal rectification (see, e.g., Lam et al., 2004, and references therein).

### 3 Harmonic analysis of observed records

10 The data presented in the previous section cover a time-span of 24.5 h. This is obviously too short to resolve distinct semi-diurnal constituents such as the lunar component  $M_2$  and the solar  $S_2$ , let alone various diurnal constituents such as  $K_1$ ,  $O_1$  and those due to subharmonic resonance, which moreover are close to the inertial period at this latitude (see the discussion in the Introduction). In the following analysis, we therefore lump nearby constituents together, and distinguish only the categories “diurnal”, “semi-diurnal”, “quarter-diurnal”, and a constant “residual”.

15 Let the original field  $q_{or}$  (standing for current components, buoyancy etc.) be approximated by the superposition

$$q = \sum_n a_n \sin(\sigma_n t - \phi_n), \quad (2)$$

20 where  $\sigma_n$  are the frequencies  $\sigma_0=0$  (residual),  $\sigma_1=7.292 \times 10^{-5}$  ( $K_1$ , diurnal),  $\sigma_2=1.405 \times 10^{-4}$  ( $M_2$ , semi-diurnal), and  $\sigma_3=2.810 \times 10^{-4} \text{ rad s}^{-1}$  ( $M_4$ , quarter-diurnal). Here the amplitudes  $a_n$  and phases  $\phi_n$  are given by

$$a_n = 2 \left( \langle q \sin \sigma_n t \rangle^2 + \langle q \cos \sigma_n t \rangle^2 \right)^{1/2};$$

$$\tan \phi_n = -\langle q \cos \sigma_n t \rangle / \langle q \sin \sigma_n t \rangle,$$

### Internal tides and energy fluxes over Great Meteor Seamount

T. Gerkema and  
H. van Haren

[Title Page](#)

[Abstract](#)

[Introduction](#)

[Conclusions](#)

[References](#)

[Tables](#)

[Figures](#)

[|◀](#)

[▶|](#)

[◀](#)

[▶](#)

[Back](#)

[Close](#)

[Full Screen / Esc](#)

[Printer-friendly Version](#)

[Interactive Discussion](#)

where  $\langle \cdot \rangle$  stands, as before, for time-averaging over the whole record. In this procedure, we treat different constituents as if they were orthogonal, mimicking a Fourier decomposition. The validity of this procedure can be checked a posteriori by comparing the original signal  $q_{or}$  with the sum (2); we carried out such checks and found that the two were always very similar (an example is shown in Fig. 6).

We present the results of this decomposition for the cross-slope and along-slope currents. The residual (i.e. time-averaged) flow is shown in Fig. 5; it confirms the presence of a flow that is predominantly directed off the seamount in the upper layer, as noticed above already. As usual, we split the time-dependent constituents (i.e., diurnal, semi-diurnal and quarter-diurnal) into two parts: a depth-averaged, or barotropic part, and the remainder, or baroclinic part. The barotropic cross-slope flow is shown in Fig. 6. Amplitudes are: 0.02 (semi-diurnal), 0.0075 (diurnal), and 0.0024 (quarter-diurnal), all in  $\text{m s}^{-1}$ . The semi-diurnal constituent is 2.7 times stronger than the diurnal one. This factor falls within the range of values observed by [Mohn and Beckmann \(2002\)](#), who found the following typical values for the tidal/inertial constituents (all in  $\text{m s}^{-1}$ ):  $M_2$ , 0.14;  $S_2$ , 0.04;  $K_1/f$ , 0.03;  $O_1$ , 0.02. The diurnal components together thus are 2 to 3.6 times smaller than the semi-diurnal ones, depending on the moment within the spring-neap cycle. Our measurements were in fact made approximately half-way between first-quarter and full moon, so that the two are in agreement. We note that [Mohn and Beckmann \(2002\)](#) found also that the diurnal components are strongly enhanced near the seamount; in the neighbouring open ocean, they form a much smaller fraction (order one-tenth) of the total tidal signal.

The remainder being the baroclinic tidal signal, we determine its amplitude  $a$  and phase  $\phi$  as indicated above. The results for the cross-slope component  $u$  are shown in Figs. 7a, d. The semi-diurnal constituent (solid line) has its largest amplitudes in the upper 500 m of the watercolumn, and is generally stronger than the other constituents, except near 300 m depth, where the diurnal signal peaks (dashed). The semi-diurnal phase shows a clear upward increase between 300–600 m depth, indicating upward phase propagation and hence downward energy propagation. The phases are here

## Internal tides and energy fluxes over Great Meteor Seamount

T. Gerkema and  
H. van Haren

[Title Page](#)

[Abstract](#)

[Introduction](#)

[Conclusions](#)

[References](#)

[Tables](#)

[Figures](#)

◀

▶

◀

▶

[Back](#)

[Close](#)

[Full Screen / Esc](#)

[Printer-friendly Version](#)

[Interactive Discussion](#)

represented in “unwrapped” angles; as a consequence, they cover intervals larger than the strictly necessary length of  $2\pi$ . (This is done for clarity of presentation; otherwise the diurnal and quarter-diurnal constituents, in particular, would give rise to highly erratic plots, due to the jumps from 0 to  $2\pi$ , and vice versa, which of course have no physical significance in themselves.)

The remaining panels of Fig. 7 show amplitudes and phases of the along-slope baroclinic current velocity  $v$ , and of buoyancy  $b$ . Overall, the phase of the semi-diurnal constituent of  $v$  lags that of  $u$  by values of around  $\pi/2$  (typically between 1.3 and 1.8 in the upper 600 m), consistent with the idea of along-slope uniformity (which we assume in Sect. 5), which implies  $v_t = -fu$  and hence gives rise to a phase shift of  $\pi/2$ . The diurnal across and along-slope components both show a distinct peak at around 300 m depth, with nearly identical amplitudes, indicative of circular polarization, as may be expected at this near-inertial frequency. As mentioned in the Introduction, various sources may be responsible for this peak; the numerical experiments, discussed in Sect. 5, suggest that the peak is not of tidal origin.

These harmonic constituents, taken together, give a reasonably faithful description of the original signal. The superposition of the semi-diurnal, diurnal, quarter-diurnal constituents deviates on average (in time and vertically) from the original baroclinic signal by  $0.012 \text{ ms}^{-1}$  for the cross-slope component (rms-value:  $0.043 \text{ ms}^{-1}$ ), by  $0.013 \text{ ms}^{-1}$  for the along-slope component (rms-value:  $0.038 \text{ ms}^{-1}$ ), and by  $6.4 \times 10^{-5} \text{ ms}^{-2}$  for buoyancy (rms-value:  $2.0 \times 10^{-4} \text{ ms}^{-2}$ ).

## 4 Energy fluxes

In the basic definition of internal-tide energy flux,

$$E_f = \langle u' p' \rangle, \quad (3)$$

where the baroclinic velocity  $u'$  can be calculated from observed profiles by subtracting the depth-averaged part, which can be presumed to represent the barotropic signal.

## Internal tides and energy fluxes over Great Meteor Seamount

T. Gerkema and H. van Haren

[Title Page](#)

[Abstract](#)

[Introduction](#)

[Conclusions](#)

[References](#)

[Tables](#)

[Figures](#)

◀

▶

◀

▶

[Back](#)

[Close](#)

[Full Screen / Esc](#)

[Printer-friendly Version](#)

[Interactive Discussion](#)

The principal difficulty lies in finding the baroclinic pressure,  $p'$ ; we discuss this problem first.

#### 4.1 Indeterminacy in energy-flux profiles

We start with the linear hydrostatic momentum equations

$$u_t - fv = -p_x \quad (4)$$

$$v_t + fu = -p_y \quad (5)$$

$$p_z = b \quad (6)$$

where  $p$  is pressure (now divided by a constant reference value of density,  $\rho_*$ ), and  $b$  buoyancy, defined in Eq. (1). These quantities represent the barotropic plus baroclinic fields; in Eq. (6), the static fields have been left out. We note that because  $p$  is here defined as pressure divided by  $\rho_*$ , the definition of energy-flux (3) changes into  $E_f = \rho_* \langle u' p' \rangle$ .

To calculate the internal-tide energy flux, we need to distill first their baroclinic parts (denoted by primes). For the horizontal velocity components, we do so by subtracting the depth-average values:

$$u' = u - \frac{1}{h} \int_{-h}^0 dz u; \quad v' = v - \frac{1}{h} \int_{-h}^0 dz v. \quad (7)$$

Here the surface is placed at  $z=0$ , and the bottom at  $z=-h(x, y)$ ; we do not assume uniform depth. By construction, the vertical integrals of  $u'$  and  $v'$  are zero, a property we may refer to as the “baroclinicity condition for velocity”.

The other baroclinic quantity we need is pressure  $p'$ , which is related to  $b'$  via the hydrostatic balance,  $p'_z = b'$ . For the moment we shall suppose we have been able to determine  $b'$  (we return to this point in Sect. 4.2), and focus henceforth on deriving  $p'$  from it.

#### Internal tides and energy fluxes over Great Meteor Seamount

T. Gerkema and  
H. van Haren

[Title Page](#)

[Abstract](#)

[Introduction](#)

[Conclusions](#)

[References](#)

[Tables](#)

[Figures](#)

◀

▶

◀

▶

[Back](#)

[Close](#)

[Full Screen / Esc](#)

[Printer-friendly Version](#)

[Interactive Discussion](#)

The hydrostatic balance implies

$$p'(t, x, y, z) = p'(t, x, y, z_0) + \int_{z_0}^z d\bar{z} b'(t, x, y, \bar{z}), \quad (8)$$

where the first term on the right is a “constant” of integration; the value of  $z_0$  is arbitrary, but natural choices are  $z_0=0$  (surface) or  $z_0=-h(x, y)$  (bottom).

5 Garcia Lafuente et al. (1999) took the former, but neglected, without justification, the constant of integration. This amounts to assuming that baroclinic pressure vanishes at the surface, an assumption rightly criticized by Kunze et al. (2002). (We note that baroclinic surface pressure does not even vanish under the rigid-lid approximation – assuming it does is an elementary misconception that occasionally surfaces in the literature.)

10 The central problem – to determine the constant of integration – thus remains. To solve this, Kunze et al. (2002) proposed a “baroclinicity condition for pressure”, stating that the vertically integrated baroclinic pressure must be zero; this would indeed fix the constant. However, this condition is in general incompatible with the other baroclinicity 15 condition, that for velocity – except in the absence of topography (i.e. if the bottom is purely horizontal). This point seems to have passed unnoticed in the literature, but it is in fact easy to prove. To begin with, it is clear from Eqs. (4) and (5), applied to the baroclinic fields, that the baroclinicity condition for velocity implies

$$\int_{-h}^0 dz p'_x = 0; \quad \int_{-h}^0 dz p'_y = 0. \quad (9)$$

20 Thus, the vertically integrated *horizontal derivatives* of baroclinic pressure vanish. Moreover, we have the mathematical identity

$$\frac{\partial}{\partial x} \int_{-h(x,y)}^0 dz p' = p'|_{z=-h} h_x + \int_{-h(x,y)}^0 dz p'_x \quad (10)$$

(and an analogous expression in terms of the  $y$  derivative). The second term on the right is zero because of Eq. (9). The first term on the right, however, contains the

Internal tides and  
energy fluxes over  
Great Meteor  
Seamount

T. Gerkema and  
H. van Haren

[Title Page](#)

[Abstract](#)

[Introduction](#)

[Conclusions](#)

[References](#)

[Tables](#)

[Figures](#)

[◀](#)

[▶](#)

[◀](#)

[▶](#)

[Back](#)

[Close](#)

[Full Screen / Esc](#)

[Printer-friendly Version](#)

[Interactive Discussion](#)

baroclinic pressure at the bottom, which in general is not zero. It thus follows that, in the presence of topography, the vertically integrated baroclinic pressure cannot be assumed to be zero. In fact, even if the baroclinic bottom pressure were assumed to be zero, it may still be inconsistent to require the vertically integrated pressure to be zero, because this requirement may yield a profile in which the value at the bottom is nonzero, contradicting the original assumption.

In the absence of any topography, on the other hand, we can write the baroclinic vertical velocity as a sum of modes  $W_n(z) \exp i(k_n x + l_n y - \sigma t)$  (summing over mode number  $n$ ), in which case the baroclinic pressure and horizontal velocities are all proportional to its derivative  $W'_n(z)$ ; it then follows immediately that the vertical integrals of these quantities must be zero (since  $W$  vanishes at the surface and bottom).

The underlying cause why the presence of a slope spoils the “baroclinicity condition for pressure” proposed by [Kunze et al. \(2002\)](#), lies in the non-separable nature of the problem. In the absence of topography, separation of horizontal and vertical coordinates applies, and one can deal with the vertical structure independently of the horizontal position. In the presence of topography, the two become intertwined. Indeed, it is clear from Eq. (8) that one could find the “constant” of integration, which is due to vertical integration, from information of the horizontal dependence of velocity. (Specifically, taking  $z_0=0$ , one could find the constant by horizontally integrating Eqs. (4) and (5), with respect to  $x$  and  $y$ , respectively.) But from measurements at a single station, such information is simply not available.

As the problem seems to be fundamentally unsolvable, this leaves us no other choice than a pragmatic approach. As a matter of fact, in its source region, i.e. over the slope, the internal tide is usually concentrated in beams. Suppose, for example, that the beam is located in the upper layer of the water column, and that baroclinic currents are very weak in the lower layer; then it makes sense to assume that all baroclinic fields, including pressure, are weak there. One may then simply assume the baroclinic pressure at the bottom to be zero.

To see how the choice of the level of zero pressure affects the energy-flux profiles,

## Internal tides and energy fluxes over Great Meteor Seamount

T. Gerkema and  
H. van Haren

[Title Page](#)

[Abstract](#)

[Introduction](#)

[Conclusions](#)

[References](#)

[Tables](#)

[Figures](#)

◀

▶

◀

▶

[Back](#)

[Close](#)

[Full Screen / Esc](#)

[Printer-friendly Version](#)

[Interactive Discussion](#)

we consider three cases, all for the semi-diurnal internal tide (Fig. 8). (At this stage we ignore the barotropic contribution in  $b$ , and simply assume the observed  $b$  to be entirely baroclinic, i.e.,  $b'=b$ ; we return to this point below.) The solid line is based on the assumption of zero-integrated pressure as proposed by Kunze et al. (2002).  
5 Assuming baroclinic pressure to be zero at the bottom gives a somewhat different curve (dash-dot); both show however a clear negative flux in the upper 500 m, i.e. directed away from the seamount, as one would expect because internal tides are generated near the top of the seamount, and, according to Fig. 7a (solid line), the semi-diurnal cross-slope signal is particularly strong in the upper 500 m. It is for this reason that the  
10 dotted curve in Fig. 8 should be rejected as unphysical; it is based on the assumption of zero surface pressure.

We emphasize that the constant of integration affects only the energy-flux *profiles*, not their vertically integrated values, since the first term on the right-hand side of Eq. (8) plays no role in the vertically integrated  $u'p'$ , by virtue of the baroclinicity condition for  
15 velocity. Indeed, for each of the three profiles in Fig. 8, the integrated value is the same, namely  $-2.4 \text{ kW m}^{-1}$ .

## 4.2 Results

The buoyancy field shown in Figs. 3 and 7c, f contains a baroclinic as well as a barotropic tidal signal; the latter (which we denote by  $B$ ) represents merely the movement of the isopycnals that is kinematically induced by the barotropic tidal flow over the slope. To calculate the baroclinic energy flux properly, this barotropic part should be removed. It can however not be directly deduced from the data, and some additional assumptions are needed. We assume that the barotropic cross-slope flux is spatially constant; hence, for each tidal constituent, the cross-slope barotropic velocity can be  
20 written as  $U=Q \sin(\sigma t - \Phi)/h(x)$ , where  $Q$  is the amplitude of the barotropic cross-slope  
25

## Internal tides and energy fluxes over Great Meteor Seamount

T. Gerkema and  
H. van Haren

[Title Page](#)

[Abstract](#)

[Introduction](#)

[Conclusions](#)

[References](#)

[Tables](#)

[Figures](#)

[◀](#)

[▶](#)

[◀](#)

[▶](#)

[Back](#)

[Close](#)

[Full Screen / Esc](#)

[Printer-friendly Version](#)

[Interactive Discussion](#)

flux. By continuity, the vertical barotropic component then becomes

$$W = \frac{zQ \sin(\sigma t - \Phi)}{h(x)^2} h_x$$

The barotropic part of buoyancy is then given by  $B_t = -N^2 W$ . At the measurement site,  $dh/dx \approx 0.14$ . The remaining parameters ( $Q, \Phi$ ) follow from the harmonic analysis.

5 This allows to remove the barotropic part  $B$  from  $b$ . The correction thus made, however, is small; for example, for the semi-diurnal component the amplitude of  $b$  changes, on average, by only  $4 \times 10^{-5} \text{ ms}^{-2}$ .

Next we integrate  $b' = b - B$  vertically to obtain baroclinic pressure, following Eq. (8), and then, by the procedure described in the previous section, the vertically integrated 10 energy flux. The results are:  $-2.3$  (semi-diurnal),  $+0.12$  (diurnal) and  $+0.049$  (quarter-diurnal), all in  $\text{kW m}^{-1}$ ; negative (positive) means a net flux away from (towards) the seamount. The magnitude of the semi-diurnal flux is slightly smaller than the value given at the end of the previous section; this is because we have here properly calculated  $b' = b - B$ , whereas the earlier value was simply based on the assumption that  $B$  is 15 negligible. The diurnal and quarter-diurnal flux are both directed toward the seamount; the latter may in fact be regarded as unreliable (and is ignored hereafter), since the current velocities found for the quarter-diurnal component fall largely within the error of the harmonic fit (cf. the deviations stated at the end of Sect. 3). To shed more light on the semi-diurnal and diurnal components, we consider results from numerical 20 experiments.

## 5 Numerical modelling

We compare the energy fluxes obtained from the yoyo measurements with those from a linear hydrostatic internal-tide model that was previously used to estimate energy fluxes in the Bay of Biscay (Gerkema et al., 2004); the model assumes uniformity 25 in the along-slope direction. The required input consists of three things: a vertical

---

Internal tides and  
energy fluxes over  
Great Meteor  
Seamount

T. Gerkema and  
H. van Haren

---

[Title Page](#)

[Abstract](#)

[Introduction](#)

[Conclusions](#)

[References](#)

[Tables](#)

[Figures](#)

[◀](#)

[▶](#)

[◀](#)

[▶](#)

[Back](#)

[Close](#)

[Full Screen / Esc](#)

[Printer-friendly Version](#)

[Interactive Discussion](#)

## Internal tides and energy fluxes over Great Meteor Seamount

T. Gerkema and  
H. van Haren

[Title Page](#)

[Abstract](#)

[Introduction](#)

[Conclusions](#)

[References](#)

[Tables](#)

[Figures](#)

[|◀](#)

[▶|](#)

[◀](#)

[▶](#)

[Back](#)

[Close](#)

[Full Screen / Esc](#)

[Printer-friendly Version](#)

[Interactive Discussion](#)

profile of buoyancy frequency  $N$ , for which we use Fig. 2c; a topographic profile, for which we use the track shown in Fig. 1; and the cross-slope barotropic current fluxes ( $Q$ ). The latter can be derived from the barotropic current amplitudes mentioned in Sect. 3 (see also Fig. 6), by multiplying with the local waterdepth (1980 m); this gives

5  $Q=39.6$  (semi-diurnal) and  $14.9$  (diurnal), both in  $\text{m}^2 \text{s}^{-1}$ . The resulting pattern for the semi-diurnal tide, in terms of the amplitude of baroclinic  $u'$ , is shown in Fig. 9. The lower panel shows the corresponding amplitude profile of  $u'$  at the location of the yoyo-station; this profile is to be compared with the observed one (thin line). In both, the largest amplitudes occur in the upper 200 m, but the observed signal has a  
10 much smaller amplitude and is much wider, in other words, it is more smeared out than the beam in the numerical model. These effects of amplitude reduction and widening partly compensate each other in a depth-integrated sense. This becomes apparent if one calculates the vertically integrated energy-flux, which is  $-2.6 \text{ kWm}^{-1}$ , being only 13% larger in magnitude than the observed value (which was  $-2.3 \text{ kWm}^{-1}$ ).

15 For the diurnal component, the signal is much weaker (Fig. 10), since the cross-slope barotropic component, which determines the forcing, is about 2.6 times weaker. The energy flux is here predominantly negative: the model yields a vertically integrated energy flux of  $-0.034 \text{ kWm}^{-1}$ , consistent with the idea of internal-tide propagation away from the seamount. Recall that the observed value was positive, and moreover much  
20 larger:  $+0.12 \text{ kWm}^{-1}$ . Part of the explanation may lie in the fact that in the observed results, near-inertial internal waves dominate the “diurnal” signal, which are not due to barotropic tidal forcing and hence not reproduced by the model.

## 6 Conclusions

25 In this paper we have focussed on the vertically integrated energy fluxes instead of their vertical profiles, because the latter are fundamentally ambiguous over topographic features, as argued in Sect. 4.1. Over a sloping bottom the “baroclinicity condition for pressure”, as proposed by [Kunze et al. \(2002\)](#), fails to be valid. This failure is

frustrating, since the primary interest of internal-tide energy fluxes lies in regions of strong topography! Fortunately, the vertically integrated values can be determined unambiguously.

We found that the observed semi-diurnal internal-tide energy flux is very similar to the one found from a numerical model; also the location of large amplitudes is correctly modelled, but the model represents the internal tide as a more intense, peaked beam than is found in the observations. The differences between model and observations are much larger for the diurnal signal, which at this latitude coincides with near-inertial signal. Indeed the observations yield a northward energy flux, i.e. towards the seamount, which is not only directionally opposed to the model result, but also much larger in amplitude. This is plausibly due to the fact that the mechanisms behind near-inertial waves (primarily the wind) are not included in the model. Still another mechanism may be responsible for the enhanced diurnal/inertial signal, namely parametric instability of the  $S_2$  tide, creating a subharmonic (which is not included in the model, either).

The semi-diurnal internal-tide energy flux, according to model and observations, is smaller than found for example in the Bay of Biscay, but only by factor of four. The underlying reason is that the plateau of Great Meteor Seamount, although obviously deeper than the shelf in the Bay of Biscay, still lies high enough for the slope to cross the permanent pycnocline, which was earlier shown to be a major factor in internal-tide generation (Gerkema et al., 2004).

*Acknowledgements.* We gratefully acknowledge the help of the crew on R/V Pelagia; the data was made ready for use by M. Hiehle (CTD) and Kees Veth (LADCP). The cruise during which these measurements were made forms part of the LOCO-project (NWO-groot) and BSIK. T. Gerkema receives funding from the NWO/ALW project CLIMA-DIM.

## 25 References

Dietrich, G.: Ozeanographie – physische Geographie des Weltmeeres, Georg Westermann Verlag, Braunschweig, 1970. 373

---

## Internal tides and energy fluxes over Great Meteor Seamount

T. Gerkema and  
H. van Haren

---

[Title Page](#)

[Abstract](#)

[Introduction](#)

[Conclusions](#)

[References](#)

[Tables](#)

[Figures](#)

[◀](#)

[▶](#)

[◀](#)

[▶](#)

[Back](#)

[Close](#)

[Full Screen / Esc](#)

[Printer-friendly Version](#)

[Interactive Discussion](#)

Egbert, G. D. and Ray, R. D.: Semi-diurnal and diurnal tidal dissipation from TOPEX/Poseidon altimetry, *Geophys. Res. Lett.*, 30, 1907, doi:10.1029/2003GL017676, 2003. [372](#)

Feistel, R. and Hagen, E.: On the GIBBS thermodynamic potential of seawater, *Progr. Oceanogr.*, 36, 249–327, 1995. [376](#)

5 Garcia Lafuente, J., Sarhan, T., Vargas, M., Vargas J. M., and Plaza, F.: Tidal motions and tidally-induced fluxes through La Linea submarine canyon, western Alboran Sea, *J. Geophys. Res.*, 94, 18 185–18 194, 1999. [381](#)

Gerkema, T., Lam, F. P. A., and Maas, L. R. M.: Internal tides in the Bay of Biscay: conversion rates and seasonal effects, *Deep-Sea Res. II*, 51, 2995–3008, 2004. [384](#), [386](#)

10 Gerkema, T. and Shrira, V. I.: Near-inertial waves on the “non-traditional”  $\beta$  plane, *J. Geophys. Res.*, 110, C01003, doi:10.1029/2004JC002519, 2005. [374](#)

Gerkema, T., Staquet, C., and Bouruet-Aubertot, P.: Decay of semi-diurnal internal-tide beams due to subharmonic resonance, *Geophys. Res. Lett.*, 33, L08604, doi:10.1029/2005GL025105, 2006. [373](#)

15 Hibiya, T., Nagasawa, M., and Niwa, Y.: Nonlinear energy transfer within the oceanic internal wave spectrum at mid and high latitudes, *J. Geophys. Res.*, 107(C11), 3207, doi:10.1029/2001JC001210, 2002. [373](#)

Klymak, J. M., Moum, J. N., Nash, J. D., Kunze, E., Girton, J. B., Carter, G. S., Lee, C. M., Sanford, T. B., and Gregg, M. C.: An estimate of tidal energy lost to turbulence at the Hawaiian Ridge, *J. Phys. Oceanogr.*, 36, 1148–1164, 2006. [372](#)

20 Kunze, E., Rosenfeld, L. K., Carter, G. S., and Gregg, M. C.: Internal waves in Monterey Submarine Canyon, *J. Phys. Oceanogr.*, 32, 1890–1913, 2002. [374](#), [381](#), [382](#), [383](#), [385](#)

Lam, F. P. A., Maas, L. R. M., and Gerkema, T.: Spatial structure of tidal and residual currents as observed over the shelf break in the Bay of Biscay, *Deep-Sea Res. I*, 51, 1075–1096, 2004. [377](#)

25 MacKinnon, J. A. and Winters, K. B.: Subtropical catastrophe: Significant loss of low-mode tidal energy at 28.9° N, *Geophys. Res. Lett.*, 32, L15605, doi:10.1029/2005GL023376, 2005. [373](#)

Mohn, C. and Beckmann, A.: The upper ocean circulation at Great Meteor Seamount. Part 30 I: Structure of density and flow fields, *Ocean Dynamics*, 52, 179–193, doi:10.1007/s10236-002-0017-4, 2002. [373](#), [377](#), [378](#)

Nash, J. D., Alford, M. H., and Kunze, E.: Estimating internal wave energy fluxes in the ocean, *J. Atmos. Oceanic Technol.*, 22, 1551–1570, 2005. [374](#)

## Internal tides and energy fluxes over Great Meteor Seamount

T. Gerkema and  
H. van Haren

[Title Page](#)

[Abstract](#)

[Introduction](#)

[Conclusions](#)

[References](#)

[Tables](#)

[Figures](#)

[◀](#)

[▶](#)

[◀](#)

[▶](#)

[Back](#)

[Close](#)

[Full Screen / Esc](#)

[Printer-friendly Version](#)

[Interactive Discussion](#)

Nash, J. D., Kunze, E., Lee, C. M., and Sanford, T. B.: Structure of the baroclinic tide generated at Kaena Ridge, Hawaii, *J. Phys. Oceanogr.*, 36, 1123–1135, 2006. [372](#), [374](#)

Rainville, L. and Pinkel, R.: Baroclinic energy flux at the Hawaiian Ridge: observations from the R/P *FLIP*, *J. Phys. Oceanogr.*, 36, 1104–1122, 2006. [372](#)

5 Smith, W. H. F. and Sandwell, D. T.: Global sea floor topography from satellite altimetry and ship depth soundings, *Science*, 277, 1956–1962, 1997. [389](#)

van Haren, H.: Details of stratification in a sloping bottom boundary layer of Great Meteor Seamount, *Geophys. Res. Lett.*, 32, L07606, doi:10.1029/2004GL022298, 2005. [373](#)

10 van Haren, H.: Cruise report bsik/LOCO-IW06: R.V. Pelagia cruise 64PE248, 17 May–12 June 2006, NIOZ, 2006. [375](#)

van Haren, H., Groenewegen, R., Laan, M., and Koster, B.: High sampling rate thermistor string observations at the slope of Great Meteor Seamount, *Ocean Sci.*, 1, 17–28, 2005, <http://www.ocean-sci.net/1/17/2005/>. [373](#)

15 Zaron, E. D. and Egbert, G. D.: Estimating open-ocean barotropic tidal dissipation: the Hawaiian Ridge, *J. Phys. Oceanogr.*, 36, 1019–1035, 2006. [372](#)

## Internal tides and energy fluxes over Great Meteor Seamount

T. Gerkema and  
H. van Haren

[Title Page](#)

[Abstract](#)

[Introduction](#)

[Conclusions](#)

[References](#)

[Tables](#)

[Figures](#)

◀

▶

◀

▶

[Back](#)

[Close](#)

[Full Screen / Esc](#)

[Printer-friendly Version](#)

[Interactive Discussion](#)

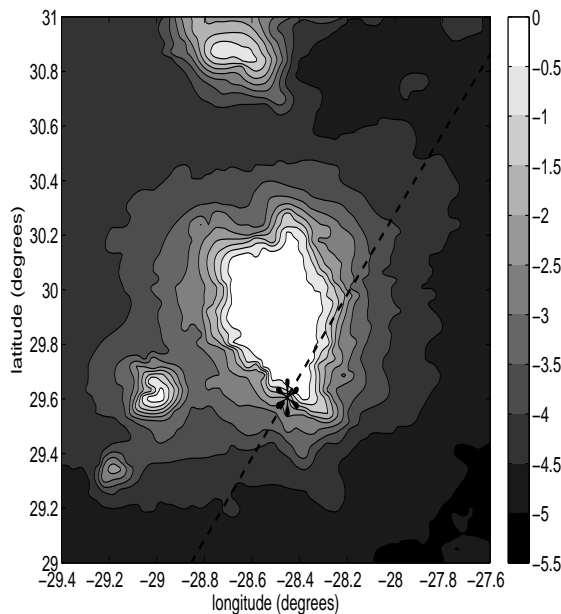


**Fig. 1.** Great Meteor Seamount, with the location of the CTD/LADCP yoyo-station at the center of the asterisk ( $29.61^{\circ}$  N,  $28.45^{\circ}$  W), and the track used in the numerical calculations indicated by the dashed diagonal. Depth is in km. This map was constructed from the database by [Smith and Sandwell \(1997\)](#). The top of the seamount is formed by a large plateau, where depths lie typically between 300 and 500 m.

## Internal tides and energy fluxes over Great Meteor Seamount

T. Gerkema and  
H. van Haren

[Title Page](#)

[Abstract](#)

[Introduction](#)

[Conclusions](#)

[References](#)

[Tables](#)

[Figures](#)

◀

▶

◀

▶

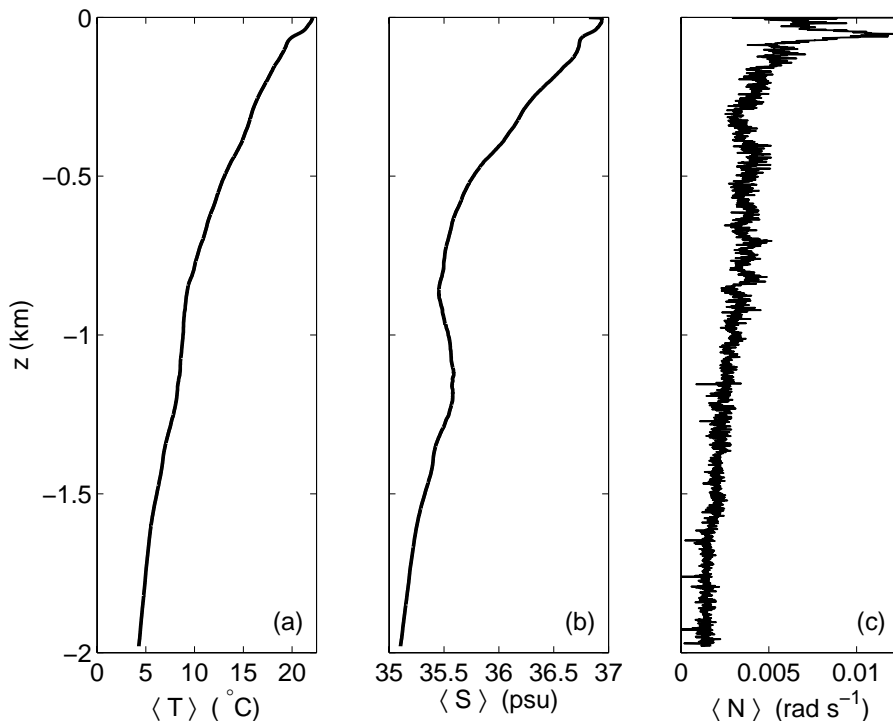
[Back](#)

[Close](#)

[Full Screen / Esc](#)

[Printer-friendly Version](#)

[Interactive Discussion](#)

**Internal tides and  
energy fluxes over  
Great Meteor  
Seamount**T. Gerkema and  
H. van Haren

**Fig. 2.** Time-averaged profiles of temperature, salinity, and buoyancy frequency, derived from the full set of CTD yoyo-casts (spanning 24.5 h).

[Title Page](#)[Abstract](#)[Introduction](#)[Conclusions](#)[References](#)[Tables](#)[Figures](#)[|◀](#)[▶|](#)[◀](#)[▶](#)[Back](#)[Close](#)[Full Screen / Esc](#)[Printer-friendly Version](#)[Interactive Discussion](#)

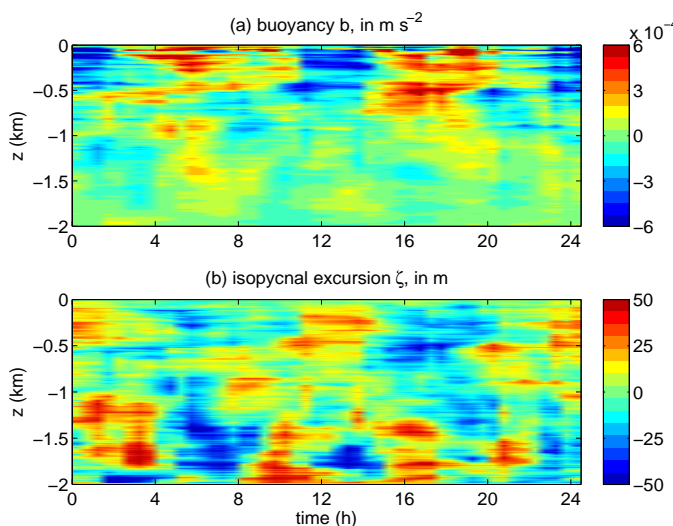


**Fig. 3.** Results derived from the CTD yoyo-casts: buoyancy  $b$ , as defined in Eq. (1), and the isopycnal excursion  $\zeta = -b/\langle N^2 \rangle$ .

## Internal tides and energy fluxes over Great Meteor Seamount

T. Gerkema and  
H. van Haren

[Title Page](#)

[Abstract](#)

[Introduction](#)

[Conclusions](#)

[References](#)

[Tables](#)

[Figures](#)

◀

▶

◀

▶

[Back](#)

[Close](#)

[Full Screen / Esc](#)

[Printer-friendly Version](#)

[Interactive Discussion](#)

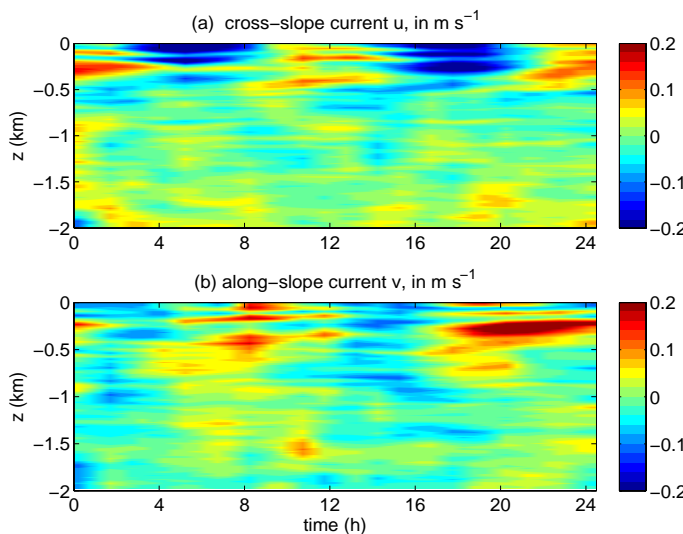


**Fig. 4.** Results from the LADCP yoyo-casts: the total cross-slope and along-slope velocity components.

## Internal tides and energy fluxes over Great Meteor Seamount

T. Gerkema and  
H. van Haren

[Title Page](#)

[Abstract](#)

[Introduction](#)

[Conclusions](#)

[References](#)

[Tables](#)

[Figures](#)

[◀](#)

[▶](#)

[◀](#)

[▶](#)

[Back](#)

[Close](#)

[Full Screen / Esc](#)

[Printer-friendly Version](#)

[Interactive Discussion](#)

Internal tides and  
energy fluxes over  
Great Meteor  
Seamount

T. Gerkema and  
H. van Haren

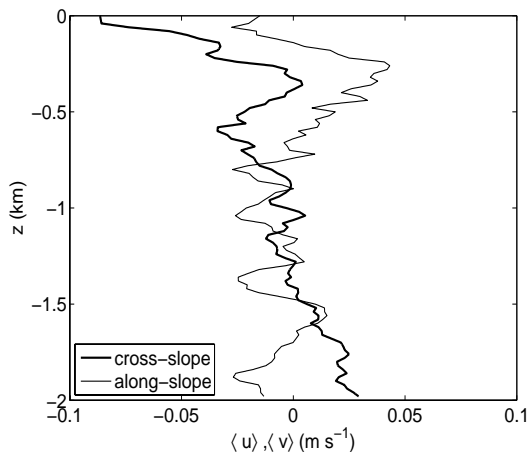


**Fig. 5.** Vertical profiles of the cross- and along-slope residual (i.e. time-averaged) currents.

[Title Page](#)

[Abstract](#)

[Introduction](#)

[Conclusions](#)

[References](#)

[Tables](#)

[Figures](#)

◀

▶

◀

▶

[Back](#)

[Close](#)

[Full Screen / Esc](#)

[Printer-friendly Version](#)

[Interactive Discussion](#)

## Internal tides and energy fluxes over Great Meteor Seamount

T. Gerkema and  
H. van Haren

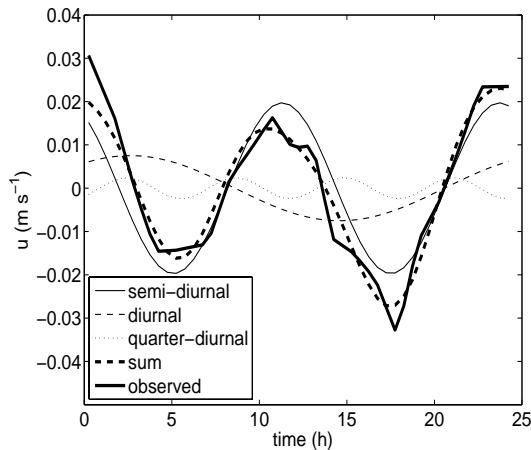


**Fig. 6.** The harmonic constituents, and their superposition, of the cross-slope barotropic flow. An indication of the accuracy of the fit is given by  $\langle|\text{sum} - \text{observed}|\rangle / \langle|\text{observed}|\rangle = 0.19$ , i.e. the fit deviates on average by 19%.

[Title Page](#)

[Abstract](#)

[Introduction](#)

[Conclusions](#)

[References](#)

[Tables](#)

[Figures](#)

◀

▶

[Back](#)

[Close](#)

[Full Screen / Esc](#)

[Printer-friendly Version](#)

[Interactive Discussion](#)

## Internal tides and energy fluxes over Great Meteor Seamount

T. Gerkema and  
H. van Haren

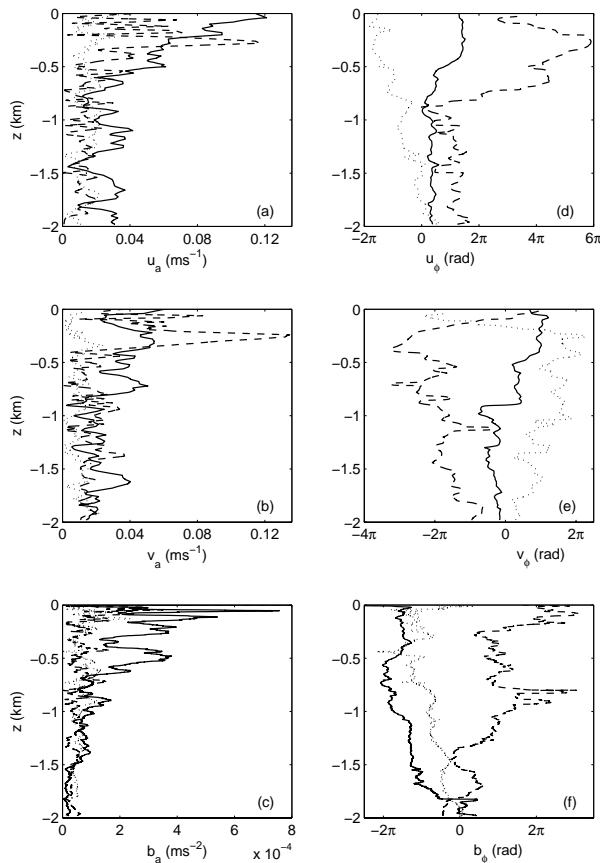


**Fig. 7.** The harmonic constituents of the cross- and along-slope baroclinic velocity ( $u$  and  $v$ , respectively), and of buoyancy  $b$ . Left panels show the amplitudes; right panels, the phases. In each panel, the semi-diurnal (solid line), diurnal (dashed), and quarter-diurnal (dots) constituents are shown.

[Title Page](#)

[Abstract](#)

[Introduction](#)

[Conclusions](#)

[References](#)

[Tables](#)

[Figures](#)

[|◀](#)

[▶|](#)

[◀](#)

[▶](#)

[Back](#)

[Close](#)

[Full Screen / Esc](#)

[Printer-friendly Version](#)

[Interactive Discussion](#)

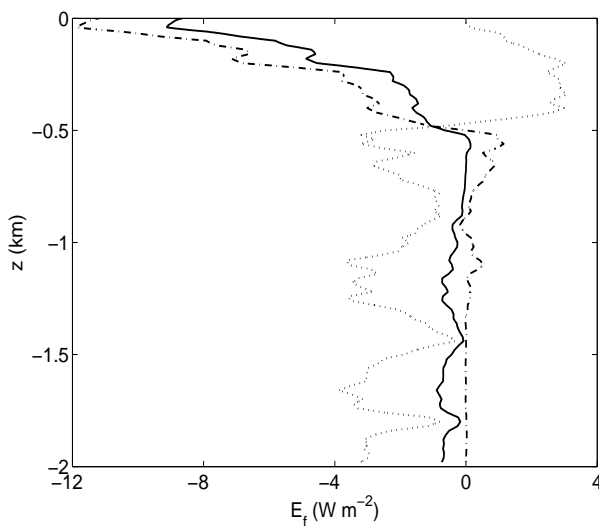


**Fig. 8.** Energy-flux profiles for the semi-diurnal internal tide, based on different ways of evaluating baroclinic pressure: assuming its vertical integral to be zero (solid line), assuming its value at the bottom or surface to be zero (dash-dot, dotted, respectively).

## Internal tides and energy fluxes over Great Meteor Seamount

T. Gerkema and  
H. van Haren

[Title Page](#)

[Abstract](#)

[Introduction](#)

[Conclusions](#)

[References](#)

[Tables](#)

[Figures](#)

◀

▶

◀

▶

[Back](#)

[Close](#)

[Full Screen / Esc](#)

[Printer-friendly Version](#)

[Interactive Discussion](#)

## Internal tides and energy fluxes over Great Meteor Seamount

T. Gerkema and  
H. van Haren

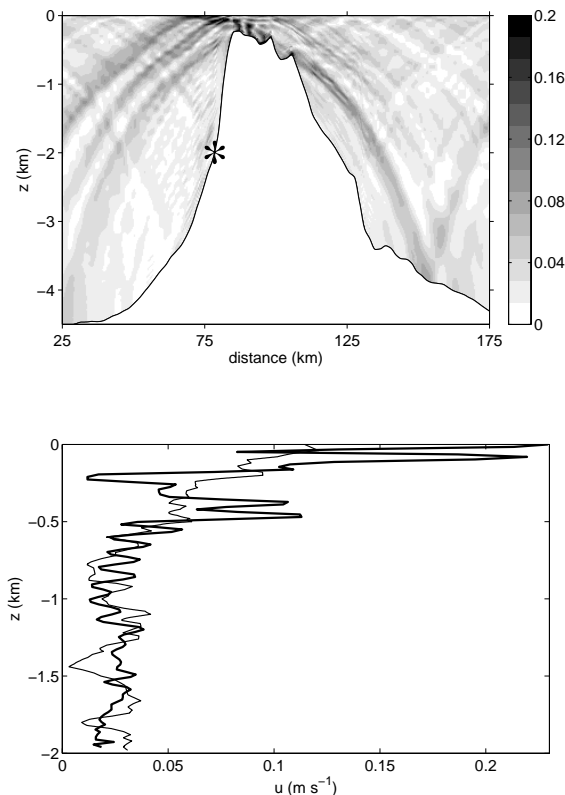


**Fig. 9.** The numerically modelled amplitude of the baroclinic semi-diurnal cross-slope current,  $u$  (in  $\text{ms}^{-1}$ ). Below, the corresponding modelled profile (thick line) at the yoyo position (marked by an asterisk above); in the same panel, the observed profile is shown (thin line), reproduced from Fig. 7a.

[Title Page](#)

[Abstract](#)

[Introduction](#)

[Conclusions](#)

[References](#)

[Tables](#)

[Figures](#)

[|◀](#)

[▶|](#)

[◀](#)

[▶](#)

[Back](#)

[Close](#)

[Full Screen / Esc](#)

[Printer-friendly Version](#)

[Interactive Discussion](#)

## Internal tides and energy fluxes over Great Meteor Seamount

T. Gerkema and  
H. van Haren

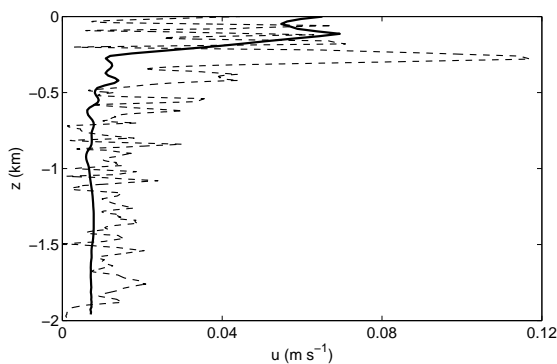
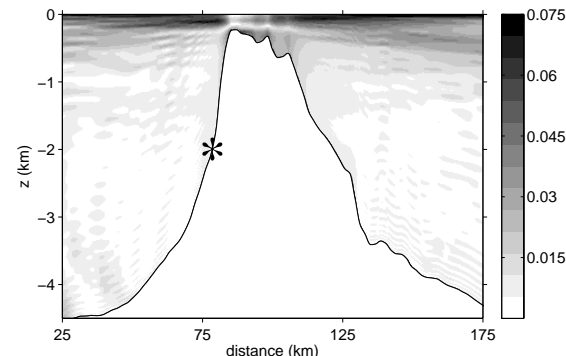


**Fig. 10.** The numerically modelled amplitude of the baroclinic diurnal cross-slope current,  $u$  (in  $\text{m s}^{-1}$ ). Below, the corresponding modelled profile (thick line) at the yoyo position (marked by an asterisk above); in the same panel, the observed profile (thin dashed line), reproduced from Fig. 7a.

[Title Page](#)

[Abstract](#)

[Introduction](#)

[Conclusions](#)

[References](#)

[Tables](#)

[Figures](#)

[|◀](#)

[▶|](#)

[◀](#)

[▶](#)

[Back](#)

[Close](#)

[Full Screen / Esc](#)

[Printer-friendly Version](#)

[Interactive Discussion](#)